

# ALMA chemical survey of disk-outflow sources in Taurus (ALMA-DOT)

## III. The interplay between gas and dust in the protoplanetary disk of DG Tau

L. Podio<sup>1</sup>, A. Garufi<sup>1</sup>, C. Codella<sup>1,2</sup>, D. Fedele<sup>1,3</sup>, K. Rygl<sup>4</sup>, C. Favre<sup>2</sup>, F. Bacciotti<sup>1</sup>, E. Bianchi<sup>2</sup>, C. Ceccarelli<sup>2</sup>, S. Mercimek<sup>1,5</sup>, R. Teague<sup>6</sup>, and L. Testi<sup>7</sup>

<sup>1</sup> INAF - Osservatorio Astrofisico di Arcetri, Largo E. Fermi 5, 50125 Firenze, Italy  
e-mail: lpodio@arcetri.astro.it

<sup>2</sup> Univ. Grenoble Alpes, CNRS, IPAG, 38000 Grenoble, France

<sup>3</sup> INAF - Osservatorio Astrofisico di Torino, Via Osservatorio 20, I-10025 Pino Torinese, Italy

<sup>4</sup> INAF - Istituto di Radioastronomia & Italian ALMA Regional Centre, via P. Gobetti 101, 40129 Bologna, Italy

<sup>5</sup> Università degli Studi di Firenze, Dipartimento di Fisica e Astronomia, Via G. Sansone 1, 50019 Sesto Fiorentino, Italy

<sup>6</sup> Center for Astrophysics | Harvard & Smithsonian, 60 Garden Street, Cambridge, MA 02138, USA

<sup>7</sup> European Southern Observatory (ESO), Karl-Schwarzschild-Str. 2, 85748, Garching, Germany

Received ...; accepted ...

### ABSTRACT

**Context.** Planets form in protoplanetary disks and inherit their chemical composition. It is therefore crucial to understand the molecular content of protoplanetary disks in their gaseous and solid components.

**Aims.** We aim to characterize the distribution and abundance of molecules in the protoplanetary disk of DG Tau and to compare it with its dust distribution.

**Methods.** In the context of the ALMA chemical survey of Disk-Outflow sources in the Taurus star forming region (ALMA-DOT) we analyse ALMA observations of the nearby disk-outflow system around the T Tauri star DG Tau in H<sub>2</sub>CO 3<sub>1,2</sub> – 2<sub>1,1</sub>, CS 5 – 4, and CN 2 – 1 emission at an unprecedented resolution of  $\sim 0''.15$ , i.e.  $\sim 18$  au at a distance of 121 pc.

**Results.** Both H<sub>2</sub>CO and CS emission originate from a disk ring located at the edge of the 1.3 mm dust continuum, with CS probing a slightly outer disk region with respect to H<sub>2</sub>CO with a peak of the emission at  $\sim 70$  and  $\sim 60$  au, and outer edge at  $\sim 130$  and  $\sim 120$  au, respectively. CN originates from an outermost and more extended disk/envelope region with a peak at  $\sim 80$  au and extends out to  $\sim 500$  au. H<sub>2</sub>CO is dominated by disk emission, while CS probes also two streams of material possibly accreting onto the disk with a peak of emission at the location where the stream connects to the disk. CN emission is barely detected and both the disk and the envelope could contribute to the emission. Assuming that all the lines are optically thin and emitted by the disk molecular layer in local thermodynamic equilibrium at temperature of 20 – 100 K, the ring- and disk-height- averaged column density of H<sub>2</sub>CO is  $2.4 - 8.6 \times 10^{13} \text{ cm}^{-2}$ , that of CS is  $1.7 - 2.5 \times 10^{13} \text{ cm}^{-2}$ , while that of CN is  $1.9 - 4.7 \times 10^{13} \text{ cm}^{-2}$ . Unsharp masking reveals a ring of enhanced dust emission at  $\sim 40$  au, i.e. located just outside the CO snowline ( $\sim 30$  au).

**Conclusions.** The finding that the CS and H<sub>2</sub>CO emission is co-spatial in the disk suggests that the two molecules are chemically linked. Both H<sub>2</sub>CO and CS may be formed in gas-phase from simple radicals and/or desorbed from grains. The observed rings of molecular emission at the edge of the 1.3 mm continuum may be due to dust opacity effects and/or continuum over-subtraction in the inner disk; as well as to increased UV penetration and/or temperature inversion at the edge of the mm-dust which would cause an enhanced gas-phase formation and desorption of these molecules at the edge of the mm dust. CN emission originates only from outside the dusty disk, therefore is even more strongly anti-correlated with the continuum, suggesting that this molecule is good probe of UV irradiation. The H<sub>2</sub>CO and CS emission originate from outside the ring of enhanced dust emission, which also coincides with a change of the linear polarization orientation at 0.87 mm (Bacciotti et al. 2018). This suggests that outside the CO snowline there could be a change of the dust properties which would reflect in the increase of the intensity (and change of polarization) of the continuum, as well as of the molecular emission.

**Key words.** Protoplanetary disks – Astrochemistry – ISM: molecules – Stars: individual: DG Tau

## 1. Introduction

With more than 4000 exoplanets discovered key open questions of modern astrophysics are to understand how planets form and what chemical composition they inherited from their natal environment. A viable way to answer these questions is to study protoplanetary disks around young Sun-like stars. The outstanding images recently obtained by the ALMA millimetre array provided the first observational indication of ongoing planet forma-

tion in less than 1 Myr old disks, through rings and gaps in their dust and gas distribution (e.g., ALMA Partnership et al. 2015; Andrews et al. 2018; de Valon et al. 2020; Favre et al. 2019; Fedele et al. 2018; Garufi et al. 2020; Sheehan & Eisner 2017, 2018). The chemical composition of the forming planets clearly depends on the spatial distribution and abundance of molecules in the disk at the time of their formation. The chemical characterisation of 0.1-1 Myr old disks is therefore crucial.

This field has been long hindered by observational difficulties due to the small sizes of disks ( $\sim 100$  au) and to the low gas-phase abundance of molecules (abundances with respect to  $\text{H}_2$  down to  $10^{-12}$ , e.g. Walsh et al. 2014). However, the number of disks imaged at high angular resolution in CO isotopologues (Booth et al. 2019b; Fedele et al. 2017; Isella et al. 2016; Zhang et al. 2020), as well as in molecules other than CO has been rapidly increasing with ALMA. In particular, ALMA allowed retrieving the radial distribution of small molecules, e.g. hydrocarbons  $\text{C}_2\text{H}$ ,  $\text{c-C}_3\text{H}_2$  (e.g., Bergin et al. 2016; Bergner et al. 2019; Kastner et al. 2015; Loomis et al. 2020; Qi et al. 2013b), nitriles CN, HCN,  $\text{HC}_3\text{N}$  (Booth et al. 2019a; Hily-Blant et al. 2017; Huang et al. 2017; Öberg et al. 2015b; van Terwisga et al. 2019),  $\text{H}_2\text{CO}$  (Qi et al. 2013a; Carney et al. 2017, 2019; Guzmán et al. 2018; Kastner et al. 2018; Loomis et al. 2015; Öberg et al. 2017; Podio et al. 2019; Pegues et al. 2020), S-bearing molecules CS,  $\text{H}_2\text{S}$ , and  $\text{H}_2\text{CS}$  (e.g., Le Gal et al. 2019; Phuong et al. 2018; Teague et al. 2018; Loomis et al. 2020), and molecular ions  $\text{N}_2\text{H}^+$ ,  $\text{DCO}^+$ ,  $\text{H}^{13}\text{CO}^+$  (e.g., Booth et al. 2019a; Carney et al. 2018; Favre et al. 2019; Mathews et al. 2013; Öberg et al. 2015a; Qi et al. 2013b). The detection of complex organic molecules is more difficult, hence only a few COMs were detected, i.e.  $\text{CH}_3\text{CN}$ ,  $\text{CH}_3\text{OH}$ , and  $\text{HCOOH}$  (Bergner et al. 2018; Favre et al. 2018; Öberg et al. 2015b; Walsh et al. 2016)), with the exception of the FU Ori-like system V883 Ori (van 't Hoff et al. 2018; Lee et al. 2019). We crucially need on one side to enlarge the census of molecules distribution in disks, and on the other side to target younger disks because planet formation may occur earlier than previously thought. These disks, however, are still partially embedded in their envelope and may be associated with molecular outflows. This requires an unprecedented combination of angular resolution and sensitivity to detect the faint emission from the disk and disentangle it from the other emitting components (e.g., the envelope and the outflow). To this aim we initiated the ALMA chemical survey of Disk-Outflow sources in the Taurus star forming region (ALMA-DOT program) (Podio et al. 2019; Garufi et al. 2020; Podio et al. 2020), which target Class I or early Class II disks associated with outflows in simple diatomic molecules (CO, CS, and CN) as well as simple organics ( $\text{H}_2\text{CO}$  and  $\text{CH}_3\text{OH}$ ) at  $\sim 20$  au resolution. The full sample, motivation, and overall results of ALMA-DOT are described in Garufi et al. in prep.

One of the sources targeted in the context of ALMA-DOT is the T Tauri star DG Tau ( $d = 121 \pm 2$  pc, Gaia Collaboration et al. 2016, 2018). DG Tau is surrounded by a compact and massive dusty disk imaged with CARMA (Isella et al. 2010) and ALMA in polarimetric mode (Bacciotti et al. 2018). Interferometric maps of CO and its isotopologues show that the envelope dominates the molecular emission on large scales (Schuster et al. 1993; Kitamura et al. 1996) while disk emission is detected on scales  $< 2''$  (Testi et al. 2002; Güdel et al. 2018; Zhang et al. 2020). The origin of the molecular emission detected with the IRAM-30m and *Herschel* (Guilloteau et al. 2013; Podio et al. 2012, 2013; Fedele et al. 2013) is unclear because DG Tau is also associated with a residual envelope and a jet (Eisloffel & Mundt 1998; Bacciotti et al. 2000). Guilloteau et al. (2013) suggest that the single-peaked profile of SO and  $\text{H}_2\text{CO}$  is due to envelope emission. However, recent ALMA observations have shown that ALMA filters out extended molecular emission from the outflow or the envelope, thus isolating the compact emission from the disk, and showed that  $\text{H}_2\text{CO}$  originates from a disk ring located at the edge of the dusty disk (Podio et al. 2019).

In this paper, we present ALMA Cycle 4 observations of CS and CN molecules in the disk of DG Tau at an unprecedented

resolution of  $\sim 0''.15$ , i.e.  $\sim 18$  au, we compare the distribution of these molecules with that of  $\text{H}_2\text{CO}$  analysed by Podio et al. (2019) and with the dust distribution and substructures, and discuss the chemistry of these species.

## 2. Observations and data products

### 2.1. Observations

ALMA observations of DG Tau were performed during Cycle 4 in August 2017 with baselines ranging from 17 m to 3.7 km (project 2016.1.00846.S, PI: L. Podio). The bandpass was calibrated with the quasar J0510+1800, and phase calibration was performed every  $\sim 8$  minutes using quasar J0438+3004. The correlator setup consists of twelve high-resolution (0.122 MHz) spectral windows (SPWs) covering several molecular transitions, among which  $\text{H}_2\text{CO}$   $3_{1,2} - 2_{1,1}$ , and several hyperfine components of the CN  $2 - 1$  transition, and one lower resolution spectral window (0.977 MHz) for the continuum covering also the CS  $5 - 4$  line (frequency,  $\nu_0$ , upper level energies,  $E_{\text{up}}$ , and line strengths,  $S_{ij}\mu^2$ , are listed in Table 1). Data reduction was carried out following standard procedures using the ALMA pipeline in CASA 4.7.2. Self-calibration was performed on the source continuum emission, by combining a selection of line-free channels, and applying the phase-solutions to the continuum-subtracted SPWs. Continuum images and spectral cubes were produced with *tclean* using an interactive mask on the visible signal until the residuals show no appreciable signal, and Briggs parameter of 0.5. The continuum subtraction is performed by estimating the continuum level from the frequency range adjacent to the targeted lines, i.e. from line-free channels. The flux calibration was performed using the quasars J0238+1636 and J0510+1800, obtaining an accuracy of  $\sim 10\%$ . The clean beam, channel width, and r.m.s. over the channel of the resulting line cubes are listed in Table 1. The continuum image has an r.m.s. of 0.12 mJy/beam.

### 2.2. Data products

Channel maps of the  $\text{H}_2\text{CO}$   $3_{1,2} - 2_{1,1}$  and CS  $5 - 4$  emission are shown in Figs. A.1. For CN  $2 - 1$ , the channel maps of the brightest hyperfine component in our spectral setting ( $N = 2 - 1$ ,  $J = 5/2 - 3/2$ ,  $F = 7/2 - 3/2$ ) is shown in Fig. A.2.

The moment 0 maps of the  $\text{H}_2\text{CO}$   $3_{1,2} - 2_{1,1}$  and CS  $5 - 4$  lines were obtained integrating the line's cubes over the velocity channels where emission above the  $3\sigma$  level is detected:  $V_{\text{LSR}} = (+3.24, +9.24) \text{ km s}^{-1}$ , i.e.  $\pm 3 \text{ km s}^{-1}$  with respect to systemic ( $V_{\text{sys}} = +6.24 \text{ km s}^{-1}$ , in agreement with Podio et al. 2013, 2019). A  $3\sigma$  clipping was applied. For CN  $2 - 1$  almost no emission above  $3\sigma$  is detected in the channel maps, therefore the moment 0 map is obtained by integrating on the same velocity interval as for  $\text{H}_2\text{CO}$  and CS and no clipping was used. The moment 0 map of CN  $2 - 1$  is due to the blending of the three hyperfine components at 226.87 GHz listed in Table 1. The velocity offset between the brightest component ( $N = 2 - 1$ ,  $J = 5/2 - 3/2$ ,  $F = 7/2 - 3/2$ ) and the two fainter ones is  $-1.47 \text{ km s}^{-1}$  and  $+0.78 \text{ km s}^{-1}$ . These offsets are smaller than the line broadening due to the disk kinematics. Therefore the moment 0 map obtained integrating on the disk velocity profile as defined for the  $\text{H}_2\text{CO}$  and CS lines ( $V_{\text{sys}} \pm 3 \text{ km s}^{-1}$ ) includes the contributions from the three components. For this reason no moment 1 map was produced for CN  $2 - 1$ . The moment 0 and 1 maps are shown in Fig. 1.

The radial intensity profiles of the lines and of the 1.3 mm continuum emission are obtained by azimuthally averaging the

**Table 1.** Properties of the observed lines and of the relative line cubes, integrated intensities and estimated column densities.

Line	$\nu_0^a$ (MHz)	$E_{\text{up}}^a$ (K)	$S_{ij}\mu^{2a}$ (D <sup>2</sup> )	clean beam (PA)	$\Delta V$ (km s <sup>-1</sup> )	r.m.s. (mJy/beam)	$F_{\text{int}}$ (mJy km s <sup>-1</sup> )	$N_X$ (10 <sup>13</sup> cm <sup>-2</sup> )
o-H <sub>2</sub> CO 3 <sub>1,2</sub> – 2 <sub>1,1</sub>	225697.775	33	43.5	0°17 × 0°13 (–20°)	0.16	1.7	210	1.8 – 5.5
CS 5 – 4	244935.557	35	19.1	0°13 × 0°10 (–9.6°)	0.6	0.6	352	1.7 – 2.5
CN 2 – 1, J=3/2–1/2, F=5/2–3/2*	226659.5584	16	4.2	0°14 × 0°12 (–7.6°)	0.16	1.5	<75	< 2 – 5
J=3/2–1/2, F=1/2–1/2	226663.6928	16	1.2					
CN 2 – 1, J=5/2–3/2, F=5/2–3/2	226874.1908	16	4.2	0°14 × 0°12 (–7.8°)	0.16	1.5	173	1.9 – 4.7
J=5/2–3/2, F=7/2–3/2*	226874.7813	16	6.7					
J=5/2–3/2, F=3/2–1/2	226875.8960	16	2.5					

<sup>a</sup> Molecular parameters from the CDMS database (Müller et al. 2001).

\* The CN 2 – 1 transition consists of 19 hyperfine structure components. The ALMA SPWs are centered on the bright hyperfine components of CN 2 – 1, indicated by \*. Because of the line broadening due to disk kinematics, each of them is blended with the adjacent hyperfine components reported in the table. The integrated line intensity refer to the sum of the blended components.

unclipped moment 0 maps after deprojecting for the disk inclination and are shown in Fig. 2.<sup>1</sup> The azimuthal average has been performed on the number of resolution elements  $N$  enclosing the full angle at separation  $r$  ( $N = 2\pi r/\text{beam}$ ). The angular resolution of the obtained intensity profiles is set by the mean beam size ( $\sqrt{B_{\text{max}} \times B_{\text{min}}} = 0''.15$  ( $\sim 18$  au),  $0''.11$  ( $\sim 14$  au), and  $0''.13$  ( $\sim 16$  au), for the H<sub>2</sub>CO, CS, and CN lines respectively), as indicated in Fig. 2.

### 3. Results

#### 3.1. Spatial distribution of H<sub>2</sub>CO, CS, and CN emission

From the moment 0 and 1 maps shown in Fig. 1 we analyse the distributions of the H<sub>2</sub>CO, CS, and CN emission in the disk of DG Tau. The map of H<sub>2</sub>CO was presented by Podio et al. (2019) who reported emission from a disk ring located at  $\sim 0''.33$ – $0''.75$  (40 – 90 au) distance from the star, at the edge of the millimeter continuum emission.

The moment 0 maps of Fig. 1 shows that the CS emission is roughly co-spatial with that of H<sub>2</sub>CO. However, the azimuthally-averaged radial profiles of Fig. 2 reveals that the ring of CS is displaced outward by  $\sim 10$  au. In fact, the H<sub>2</sub>CO emission peaks at  $\sim 60$  au and extends out to  $\sim 120$  au, while the CS emission peaks at  $\sim 70$  au and extends out to  $\sim 130$  au. The  $\sim 10$  au offset between the peaks of the H<sub>2</sub>CO and CS radial intensity profiles is larger than the uncertainty on the estimate of their position (the position of the intensity peak determined by gaussian fitting the peak profile is affected by an uncertainty of  $\sim 1/5$  of the nominal resolution imposed by the beam, i.e.  $\sim 3.6$  au for H<sub>2</sub>CO and  $\sim 3$  au for CS). Therefore, the radial offset between the H<sub>2</sub>CO and CS emission peaks is real and not due to a resolution effect. Being observed along the major axis, this effect cannot be explained by a different vertical origin for the H<sub>2</sub>CO and CS emissions. At larger radii, the CS emission probes a stream of material extending from the redshifted NW side of the disk out to  $\sim 3''$  towards the north. The NW side where this stream connects to the disk is the brightest disk region in the continuum emission (see radial cuts in Fig. B.1 of Podio et al. 2019), in polarized intensity (Fig.

2 of Bacciotti et al. 2018), and line emission. The asymmetry between the two disk sides in H<sub>2</sub>CO and CS emission is clearly seen in the moment 0 maps (Fig. 1), as well as in the line spectra obtained by integrating the line emission over the disk ring as defined by Podio et al. (2019) ( $r \sim 0''.33$  –  $0''.75$  corresponding to 40 – 90 au) (see Fig. 3), where the red-shifted peak is brighter than the blue-shifted one in both lines. The line spectra obtained by integrating the emission out to a radius of  $\sim 3''$ , i.e. over a region extending well beyond the 40 – 90 au disk ring, indicate that at larger scales this asymmetry is even more pronounced. The profiles of CN 2 – 1 and H<sub>2</sub>CO 3<sub>1,2</sub> – 2<sub>1,1</sub> integrated on  $3''$  region are similar to what observed with the IRAM-30m by Guilloteau et al. (2013). This indicates that outside the disk ring, line emission is likely dominated by the circumstellar envelope, in agreement with what suggested by Guilloteau et al. (2013).

The channel maps of the CN 2 – 1 emission at 226.87 GHz shows negative intensities in the inner disk region, i.e. for  $r < 50$  au, in the channels corresponding to the systemic velocity, for each of the three hyperfine components (see Fig. A.2). For an embedded disk like DG Tau, this is likely due to continuum over-subtraction. Circumstellar material may absorb the disk line emission at  $V_{\text{sys}}$  as well as the continuum emission at the corresponding frequency. This makes the disk continuum in the frequency channel corresponding to the systemic velocity lower than in the adjacent channels. When the operation of continuum subtraction is performed, the continuum level is extracted from the frequency range adjacent to the targeted lines. This yields a partial over-subtraction at the frequency corresponding to  $V_{\text{sys}}$ . Besides the absorption in the inner disk region, no CN 2 – 1 emission is detected in the outer disk, where continuum is fainter, and in the channels at blue- and red-shifted velocities with respect to  $V_{\text{sys}}$  which should not be affected by line/continuum absorption by the circumstellar material. Despite no clear structures are detected in the channel maps and in the moment 0 map (Figs. 1 and A.2), the azimuthally-averaged radial profile in Fig. 2 shows CN emission above the dispersion. The profile indicates that CN emission originates from a more extended region than H<sub>2</sub>CO and CS, with a peak at  $\sim 80$  au and extending out to  $\sim 500$  au. However, as the detected CN 2 – 1 emission is due to the blending of three hyperfine components, it is difficult to retrieve information on the gas kinematics and to conclude whether the CN emission is associated with the disk or it is mostly (or totally) dominated by the residual circumstellar envelope (which also acts to absorb the line/continuum emission

<sup>1</sup> With respect to Podio et al. (2019) we revise the estimate of the disk PA and inclination based on the fit of the self-calibrated continuum map obtained by stacking all the SPWs. We obtain PA = 135° and  $i = 35^\circ$ . We note, however, that the extracted azimuthally averaged radial profiles do not change significantly with respect to Podio et al. (2019).



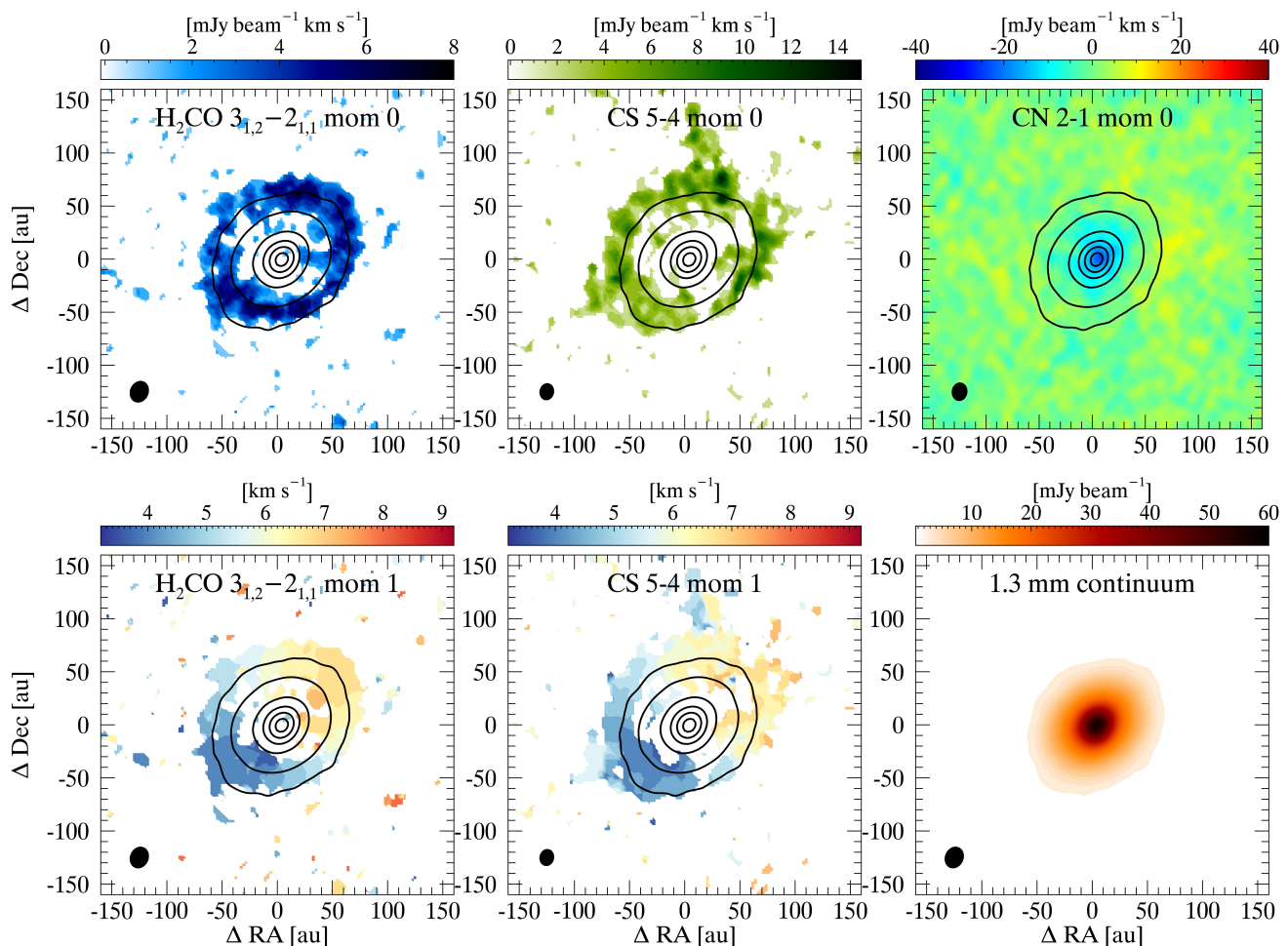


**Fig. 1.** Moment 0 maps (top panels) of  $\text{H}_2\text{CO}$   $3_{1,2} - 2_{1,1}$  (left), CS  $5 - 4$  (middle), and CN  $2 - 1$  (blending of the three components at 226.87 GHz reported in Table 1) (right) towards DG Tau. The corresponding moment 1 maps are shown in the left and middle bottom panels, while no moment 1 map is shown for CN  $2 - 1$ , due to the blending of the three hyperfine components. The bottom right panel shows the map of the continuum emission at 1.3 mm. The colour scale indicates the line intensity in  $\text{mJy beam}^{-1} \text{km s}^{-1}$  (moment 0), the velocity  $V_{\text{LSR}}$  in  $\text{km s}^{-1}$  (moment 1), and the intensity in  $\text{mJy beam}^{-1}$  (for the continuum map). The black contours indicate the 1.3 mm dust continuum emission (0.01% corresponding to the  $5\sigma$  level, 10%, 30%, 50%, 70%, and 90% contours). The ellipse in the bottom left corner of each panel shows the ALMA synthesized beam.

from the inner disk). When integrated on the disk ring between 40 – 90 au, CN shows a double-peaked profile similar to that of  $\text{H}_2\text{CO}$  and CS and consistent with disk emission (see Fig. 3). However, the spectra integrated on a  $3''$  circular area clearly indicates that the CN emission is strongly affected by extended emission from the residual envelope.

### 3.2. Dust substructures

To highlight the possible presence of dust substructures, we applied an unsharp masking filter to the continuum image at 1.3 mm as well as to that presented by Bacciotti et al. (2018) at 0.87 mm. Unsharp masking consists in subtracting from the image a blurred version of the same image in order to artificially increase the contrast (see application to disks by e.g., Quanz et al. 2011; Pérez et al. 2016). Similarly to Garufi et al. (2016), here we first divided the original image by the local variance in each pixel and then subtract the image smoothed by 60 mas. This technique revealed a ring at  $\sim 40$  au in the continuum maps at 0.87 mm and at 1.3 mm (see Fig. 4). This structure corresponds to the tentative shoulder identified by Podio et al. (2019) extract-

ing the radial intensity profile along the major axis and calculating its second derivative (see their Fig. B.1). The location where the second derivative of the intensity profile becomes negative indicating a local increase of the continuum intensity is between 38 and 44.5 au, in perfect agreement with the position of the ring revealed by applying unsharp masking. However, the precise morphology of the ring should be interpreted with caution given the arbitrariness of the technique. The barely visible outer ring in the map at 0.87 mm is an artifact of the procedure that is routinely generated at the outer edge of the detectable signal. Hence, this structure corresponds to the outer edge of the disk emission.

### 3.3. Molecules column density

In Podio et al. (2019), we computed the column density of  $\text{H}_2\text{CO}$  in the outer disk ring. Here, we followed the same procedure to constrain the column density of CS and CN. We integrated the relative emission over the same area as the  $\text{H}_2\text{CO}$  (a circular ring extending from  $0''.33$  to  $0''.75$ ) and converted this integrated flux into column density assuming local thermodynamic equilibrium (LTE) and optically thin emission through the molecular

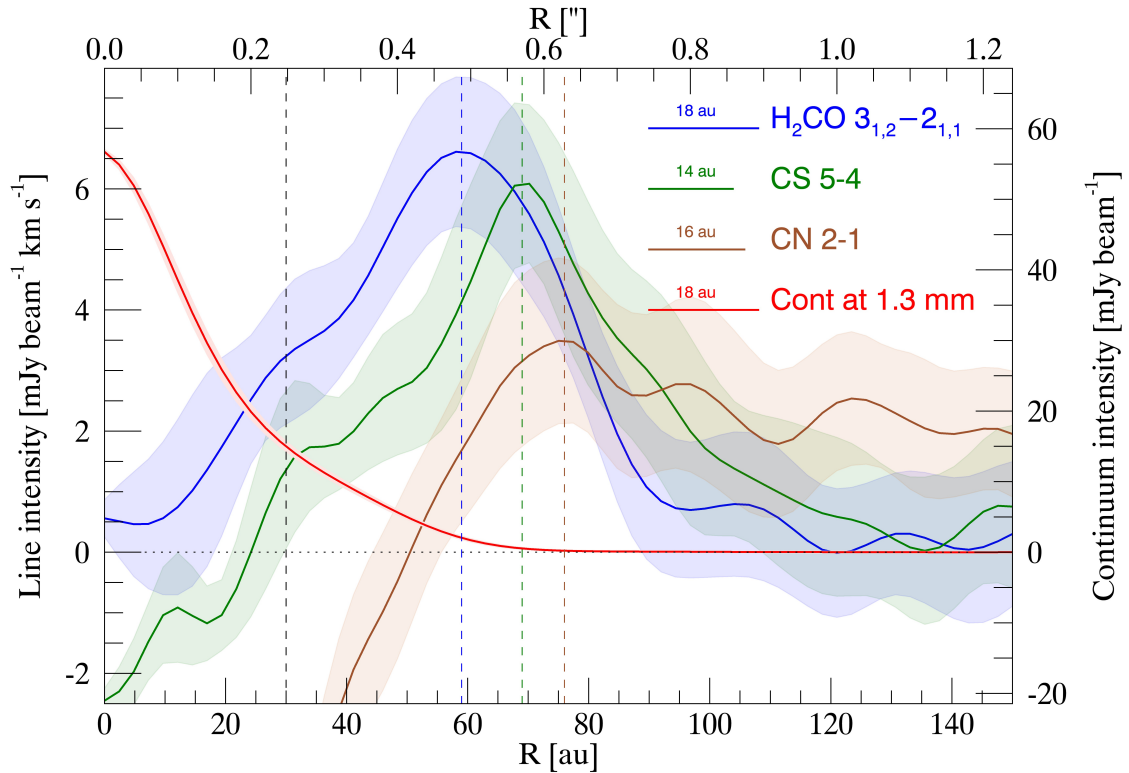


**Fig. 2.** Azimuthally-averaged radial intensity profile of  $\text{H}_2\text{CO } 3_{1,2} - 2_{1,1}$  (blue),  $\text{CS } 5 - 4$  (green), and  $\text{CN } 2 - 1$  (blending of the three components at 226.87 GHz reported in Table 1) (brown) (in  $\text{mJy beam}^{-1} \text{ km s}^{-1}$ , left axis), and of the 1.3 mm continuum (red) (in  $\text{mJy beam}^{-1}$ , right axis). The radial distance is indicated in au in the bottom axis and arcseconds in the top one. The angular resolution of the lines/continuum profiles is indicated by the corresponding horizontal lines. The shaded areas indicate the dispersion of the intensity values around the mean along each annulus in the radial direction. The vertical dashed lines indicate the position of the CO snowline (black), and of the peaks of the emission in  $\text{H}_2\text{CO } 3_{1,2} - 2_{1,1}$  (blue),  $\text{CS } 5 - 4$  (green), and  $\text{CN } 2 - 1$  (brown).

parameters and partition function from the Cologne Database of Molecular Spectroscopy (CDMS, Müller et al. 2001). The assumption of LTE is well justified as the gas density in the so-called molecular layer where the lines are thought to originate (see, e.g., Walsh et al. 2014; Öberg et al. 2017) is high (from  $\sim 10^8$  to  $\sim 10^{12} \text{ cm}^{-3}$  according to the disk model by Podio et al. 2013), i.e., well above the critical density of the considered lines (at 20 – 100 K,  $n_{\text{cr}} \sim 7.0 - 4.6 \times 10^5 \text{ cm}^{-3}$  for  $\text{H}_2\text{CO } 3_{1,2} - 2_{1,1}$ ,  $\sim 1.7 \times 10^6 - 9.5 \times 10^5 \text{ cm}^{-3}$  for  $\text{CS } 5 - 4$ , and  $\sim 2.2 \times 10^6 - 6.4 \times 10^5 \text{ cm}^{-3}$  for  $\text{CN } 2 - 1$ , Shirley 2015). Under LTE, the levels are populated according to the Boltzmann distribution and the excitation temperature is equal to the gas kinetic temperature  $T_{\text{ex}} = T_{\text{K}}$ . The temperature of the emitting layer has to be assumed as we have only one line per species. Recent multi-lines studies of CS and  $\text{H}_2\text{CO}$  emission in a few protoplanetary disks indicate that the lines originate from a disk layer at/above the CO freeze-out temperatures (Le Gal et al. 2019; Pegues et al. 2020; Teague et al. 2018). Therefore, we assume a lower range of temperatures with respect to what previously assumed in Podio et al. (2019) and compute the column density of  $\text{H}_2\text{CO}$ , CS, and CN for  $T_{\text{ex}} = T_{\text{K}} = 20 - 100 \text{ K}$ . This procedure yielded ring- and disk-height averaged column densities of  $1.8 - 5.5 \times 10^{13} \text{ cm}^{-2}$  for o- $\text{H}_2\text{CO}$ , which translates into a total column density of  $\text{H}_2\text{CO}$  of  $2.4 - 8.6 \times 10^{13} \text{ cm}^{-2}$  based on the o/p ratio estimated by Guzmán et al. (2018), of  $1.7 - 2.5 \times 10^{13} \text{ cm}^{-2}$  for CS. For CN the integrated fluxes are obtained from the moment 0 maps of the CN 2 – 1 components at 226.66 and 226.87 GHz. From the brightest lines at 226.87 GHz a column density of  $1.9 - 4.7 \times 10^{13} \text{ cm}^{-2}$  is estimated, which is consistent with

the upper limit derived from the fainter components at 226.66 GHz. The derived column density values are in agreement with the range of values found for other disks (Carney et al. 2019; Pegues et al. 2020 for  $\text{H}_2\text{CO}$ , Le Gal et al. 2019; Teague et al. 2018 for CS, and Hily-Blant et al. 2017 for CN). The integrated line intensities and the derived column densities are summarized in Table 1.

As shown by recent observational studies (Le Gal et al. 2019; Pegues et al. 2020; Teague et al. 2018) CS and  $\text{H}_2\text{CO}$  emission may be optically thick in protoplanetary disks. In order to check if and how much line opacity may affect our column density estimates, which are derived assuming optically thin emission, we converted the ring-integrated line spectra shown in Fig. 3 in brightness temperature (see Fig. B.1 in Appendix B). The line brightness temperature,  $T_{\text{B}}$ , is well below the gas temperature for optically thin lines, while it is  $\sim (0.6 - 0.8) \times T_{\text{K}}$  for thermalized lines. We find that the intensity peak of the  $\text{H}_2\text{CO } 3_{1,2} - 2_{1,1}$  and  $\text{CS } 5 - 4$  integrated spectra is  $T_{\text{B}} \sim 1.5 \text{ K}$ . This value is well below the typical gas temperatures of the  $\text{H}_2\text{CO}$  and CS emitting disk layer ( $T_{\text{ex}} \sim T_{\text{K}} \sim 11 - 37 \text{ K}$  for  $\text{H}_2\text{CO}$  (Pegues et al. 2020), and  $\sim 20 - 35 \text{ K}$  for CS (Teague et al. 2018; Le Gal et al. 2019)). Thus, we conclude that the observed lines are likely optically thin. Le Gal et al. (2019) and Pegues et al. (2020) find that the  $\text{H}_2\text{CO}$  and CS emission is mildly optically thick in the protoplanetary disks MWC 480, LKCa 15, DM Tau, and J1604-2130 (the latter two only for  $\text{H}_2\text{CO}$ ). They infer  $\tau \sim 0.07 - 0.4$  for  $\text{CS } 5 - 4$  and  $\tau \sim 0.14 - 0.85$  for the  $\text{H}_2\text{CO}$  lines with the lower upper level energies, i.e.  $E_{\text{up}} \sim 20 - 34 \text{ K}$ , hence the column densities derived using the optically thin approximation are underestimated

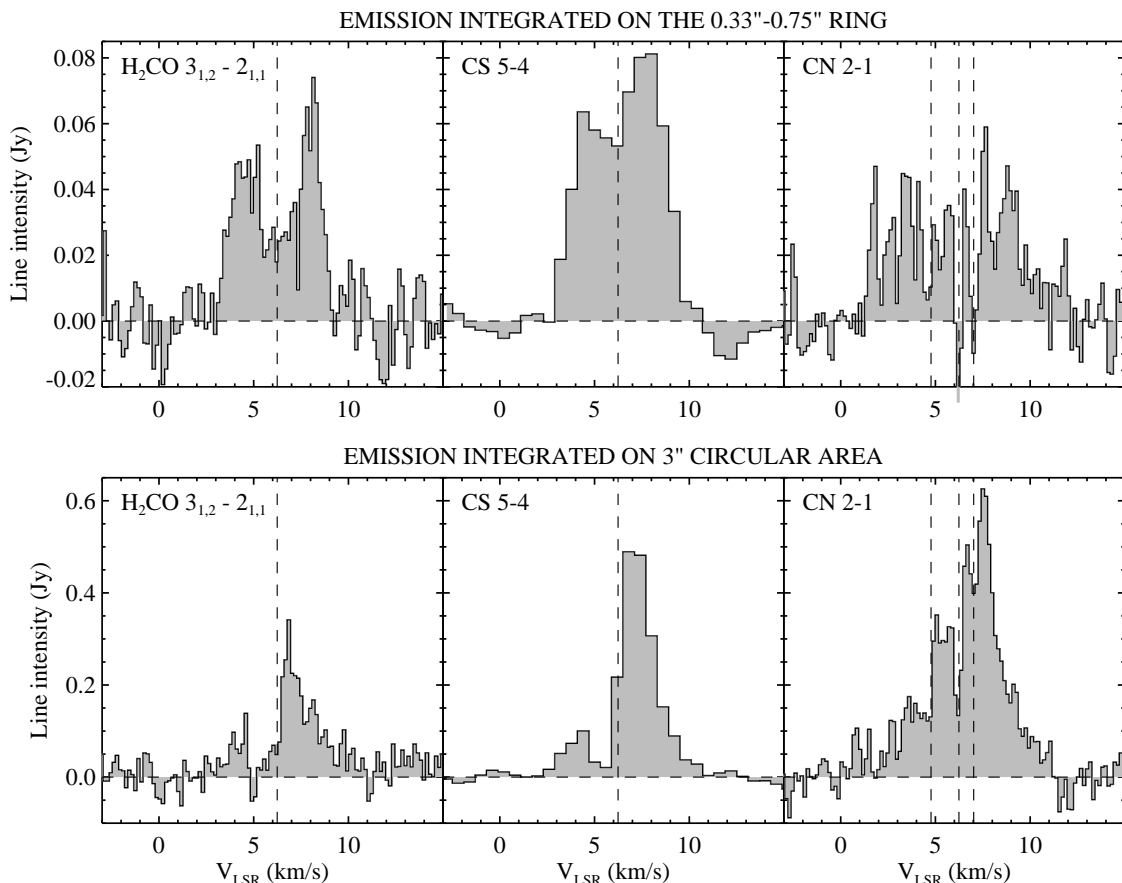


**Fig. 3.**  $\text{H}_2\text{CO}$   $3_{1,2} - 2_{1,1}$ , CS  $5 - 4$ , and CN  $2 - 1$  spectra integrated over a  $0.33'' - 0.75''$  ring area (top panels) and over a  $3''$  circular area (bottom panels). The vertical dashed lines indicate the systemic velocity,  $V_{\text{sys}} = +6.24 \text{ km s}^{-1}$ . For CN  $2 - 1$  the velocity scale corresponds to the brightest of the three hyperfine components at 226.87 GHz reported in Table 1 ( $N = 2 - 1$ ,  $J = 5/2 - 3/2$ ,  $F = 7/2 - 3/2$ ), and the position of the two fainter components is indicated by the vertical dashed lines.

by a factor of about two. As we cannot exclude that the detected  $\text{H}_2\text{CO}$  and CS emission lines are mildly optically thick in the disk of DG Tau, also our estimates of the column densities may be underestimated by a factor of a few.

## 4. Discussion

### 4.1. The origin of ring-like emission

The  $\text{H}_2\text{CO}$ , CS, and CN moment 0 maps and radial intensity profiles show that the bulk of the line emission originate from an outer disk ring while poor emission (or even negative fluxes in the case of CN and CS) is detected in the inner disk region, i.e. at radii  $\leq 50$  au. As discussed in Podio et al. (2019), the depression or lack of emission in the inner disk region may be due to: (i) lower molecular column density in the inner disk region; (ii) optically thick dust suppressing line emission; (iii) absorption of the dust continuum emission by optically thick line emission from the disk itself and/or from circumstellar material, which would then bring to an over-subtraction at the line frequency when removing the continuum evaluated in the frequency range adjacent to the line. As discussed in Sect. 3.1, the latter may be the cause of the negative values seen in the inner disk region in the channel maps, moment 0 map, radial profile and integrated spectra of CN  $2 - 1$ . Negative fluxes in the inner 20 au are seen also in the radial intensity profile of CS  $5 - 4$ , while no negative values are seen in the  $\text{H}_2\text{CO}$  profile. Following Podio et al.

(2019) we exclude that the depression in the  $\text{H}_2\text{CO}$  and CS emission is due to dust opacity for  $r > 20$  au. This is based on previous modeling of the continuum emission, which shows that the disk is optically thick in the inner 10 au. Further out, the optical depth sharply decreases to values lower than 0.5 at  $\sim 20$  au (Isella et al. 2010). Furthermore, if the inner depression was due to optically thick dust, the observed molecular rings would be centered around the continuum peak. Instead, Podio et al. (2019) noted that the  $\text{H}_2\text{CO}$  ring is displaced along the major axis with respect to the continuum and the same effect is visible in the CS map presented in this work (see Fig. 1). Finally, in the case of optically thick dust all the lines should be equally suppressed at the same radii whereas the inner profile of our lines is different (see Fig. 2), with the CO isotopologues,  $^{13}\text{CO}$  and  $\text{C}^{18}\text{O}$ , which show a smaller hole in their distribution compared to  $\text{H}_2\text{CO}$  (of  $\sim 25$  au, Güdel et al. 2018). This behavior is opposite to what was observed for DG Tau B by Garufi et al. (2020).

To conclude, while we cannot exclude the presence of  $\text{H}_2\text{CO}$  and CS emission in the inner 25 au disk region, which would remain undetected due to optically thick dust and/or continuum over-subtraction due to optically thick line emission, we confirm the presence of an outer ring of enhanced molecular emission at the edge of the mm continuum. An inner hole or dip in the distribution of  $\text{H}_2\text{CO}$  was detected also in other disks, namely TW Hya (Öberg et al. 2017), HD 163296 (Carney et al. 2017), V4046 Sgr (Kastner et al. 2018), and 5 out of 13 disks associated with  $\text{H}_2\text{CO}$  emission in the survey of Pegues et al. (2020) (two of

which are HD 163296 and V4046 Sgr). For all disks except IM Lup and HD 163296, however, optically thick dust is likely not the cause for the observed lack of  $\text{H}_2\text{CO}$  in the inner disk region, similarly to what concluded for the disk of DG Tau. Moreover, a peak of the  $\text{H}_2\text{CO}$  emission at the edge of the millimeter continuum, is found in both TW Hya and HD 163296, as well as in four of the 13 disks with detected  $\text{H}_2\text{CO}$  in the survey by Pegues et al. (2020). Concerning CS, the studies by Le Gal et al. (2019) and Loomis et al. (2020) show centrally peaked CS emission in all but one out of five disks and no emission bump at the edge of the continuum. An emission peak at the edge of the dusty disk has been reported also for other molecules, such as  $\text{DCO}^+$  and CO isotopologues (see, e.g., Favre et al. 2019; Huang et al. 2016; Öberg et al. 2017).

Concerning CN, as discussed in Sect. 3.1, almost no emission is detected in the channel maps and in the moment 0 map, but CN emission is clearly visible in the azimuthally averaged radial profile and in the integrated spectra (Figs. 2 and 3). It is not clear if the emission originates at least partially from an outer disk region or if it is mostly from the envelope. In the second case, the negative fluxes in the inner disk region could be due to absorption of the disk continuum emission by the surrounding extended envelope, which would mask any disk emission.

#### 4.2. The interplay of gas and dust

To quantify the degree of dust accumulation occurring at the location of the dust ring revealed by unsharp masking (see Fig. 4), we integrated the continuum flux encompassed in the original map at the ring location as well as the total flux from the disk. A gaussian fit to the observed emission yields a disk major axis of  $0''.45$  and a disk inclination  $i$  of  $35^\circ$ . The flux integrated over this region is 0.29 Jy whereas the ring flux amounts to 0.04 Jy. It is thus clear that this substructure is morphologically different from the bright structures recurrently imaged by ALMA (see e.g., Andrews et al. 2018). In fact, the dust ring in the disk of DG Tau only shows a  $\sim 10\%$  flux enhancement with respect to the contiguous disk regions and this converts into a comparable, and thus marginal, amount of dust accumulation (assuming that the enhanced emission is not due to changes in the dust opacity and/or temperature in the ring). The dust mass of disk and ring can be obtained from the aforementioned fluxes in the assumption of optically thin emission through:

$$M_{\text{dust}} = \frac{F_{\text{mm}} d^2}{\kappa_{\lambda} B_{\lambda}(T_{\text{dust}})} \quad (1)$$

where the dust opacity  $\kappa_{\lambda}$  at 1.3 mm is assumed to be a global  $2.3 \text{ cm}^2 \text{ g}^{-1}$  (from Beckwith et al. 1990) and the Planck function  $B_{\lambda}(T_{\text{dust}})$  is calculated from an overall dust temperature  $T_{\text{dust}}$  of 20 K. Under these assumptions, the total dust mass is  $\sim 120 M_{\oplus}$  and the ring dust mass is  $\approx 16 M_{\oplus}$ .

The dusty ring visible after unsharp masking shows spatial analogies with both the linear polarization map at 0.87 mm by Bacciotti et al. (2018) and the molecular emission presented in this work, as shown in Fig. 4. The orientation of the polarization vectors changes from parallel to the disk minor axis to azimuthal at the radial location of the ring, i.e. at  $\sim 40$  au. This confirms the suggestion given in Bacciotti et al. (2018) that sharp changes in the orientation of the polarization pattern may betray the presence of yet unseen substructures in the dust and gas distribution. Moreover, both the CS and  $\text{H}_2\text{CO}$  rings of emission of Fig. 1 lie at the outer edge of the continuum substructure. We also note that the dusty ring is located beyond the CO snowline  $R_{\text{CO}} \sim 30$

au, as computed by the thermo-chemical disk model ProDiMo (Podio et al. 2013). This suggests that outside the CO snowline there could be a change of the dust properties (e.g. dust grain size and opacity) which would reflect in (i) an enhancement of the dust continuum emission; (ii) a change of the orientation of the polarization due to dust grain self-scattering (Bacciotti et al. 2018); and (iii) an enhancement of  $\text{H}_2\text{CO}$  and CS emission.

#### 4.3. The chemical origin of detected molecules

The observed  $\text{H}_2\text{CO}$   $3_{1,2} - 2_{1,1}$  and CS  $5 - 4$  emission originate roughly from the same region of the disk radially, i.e. from a ring located between  $\sim 40$  au and  $\sim 130$  au and with a peak close to the edge of the distribution of the mm dust grains, with the CS emission displaced by  $\sim 10$  au towards the outer disk. The two transitions have very similar upper level energy and critical density ( $E_{\text{up}} = 33$  K, and 35 K, and  $n_{\text{cr}} \sim 7 - 5 \times 10^5 \text{ cm}^{-3}$ , and  $17 - 9.5 \times 10^5 \text{ cm}^{-3}$  at 20–100 K, for the  $\text{H}_2\text{CO}$  and the CS line, respectively). Therefore, they are excited at similar conditions and it is reasonable to assume that they arise from the same region of the disk also vertically, in agreement with disk modeling by Fedele & Favre (2020).

$\text{H}_2\text{CO}$  and CS could also be linked from a chemical point of view. Following Le Gal et al. (2019) the main formation routes of CS are: (i) either via rapid ion–neutral reactions between  $\text{S}^+$  and small hydrocarbons (such as  $\text{CH}_x$  and  $\text{C}_y\text{H}$ , with  $x = 1 - 4$  and  $y = 2 - 3$ ), which produces carbonated S-ions, including  $\text{HCS}^+$ ,  $\text{CS}^+$ ,  $\text{HC}_3\text{S}^+$ , and  $\text{C}_2\text{S}^+$ , that subsequently recombine with electrons to form neutral S-bearing species; (ii) or via neutral–neutral reactions between S and small hydrocarbons (at deeper disk layers). The main formation route of  $\text{H}_2\text{CO}$  in gas phase is through the reaction  $\text{CH}_3 + \text{O}$ , which is efficient in the warm inner region and molecular layers of the disk where atomic oxygen is produced by photodissociation of gas-phase CO (e.g., Willacy & Woods 2009; Loomis et al. 2015). The latter, also makes available C for the formation of small hydrocarbons which boost the formation of both  $\text{H}_2\text{CO}$  and CS. Finally, both species are easily destructed in the disk atmosphere due to photo-dissociation and reactions with protons and protonated ions (i.e., with  $\text{H}^+$ ,  $\text{H}_3^+$ , and  $\text{HCO}^+$ ), and will freeze-out onto dust grains in the disk midplane. The freeze-out will occur when the dust temperature falls below their freeze-out temperature ( $T_{\text{d}}$ ) which is  $\sim 65$  K for CS and  $\sim 90$  K for  $\text{H}_2\text{CO}$  as estimated from the binding energy by Wakelam et al. (2017) ( $E_{\text{b}}=3200$  K and 4500 K, respectively)<sup>2</sup>. Therefore, if  $\text{H}_2\text{CO}$  and CS are primarily produced in gas-phase in the disk molecular layer, their abundance would be strongly linked to the presence of small hydrocarbons, such as  $\text{CH}_3$ . On the other hand, there could be a second reservoir of  $\text{H}_2\text{CO}$  and CS due to the release from the dust grain mantles. For both  $\text{H}_2\text{CO}$  and CS the peak of emission at the edge of the millimeter continuum could be due to several mechanisms, as discussed by Carney et al. (2017); Öberg et al. (2017); Podio et al. (2019); Pegues et al. (2020): (i) enhanced photodesorption from dust grains; (ii) enhanced photodissociation of CO, which produces atomic O and small hydrocarbons for the formation of  $\text{H}_2\text{CO}$ , as well as CS; (iii) temperature inversion in the outer disk region with fewer solids.

With respect to  $\text{H}_2\text{CO}$  and CS, CN emission originates from a larger ring located outside the dusty disk, and extending from  $\sim 80$  au to  $\sim 500$  au. CN ring-like emission was detected in a few other disks, i.e. in TW Hya (Hily-Blant et al. 2017), and

<sup>2</sup> Lower binding energies and freeze-out temperatures are found by Penteado et al. (2017)



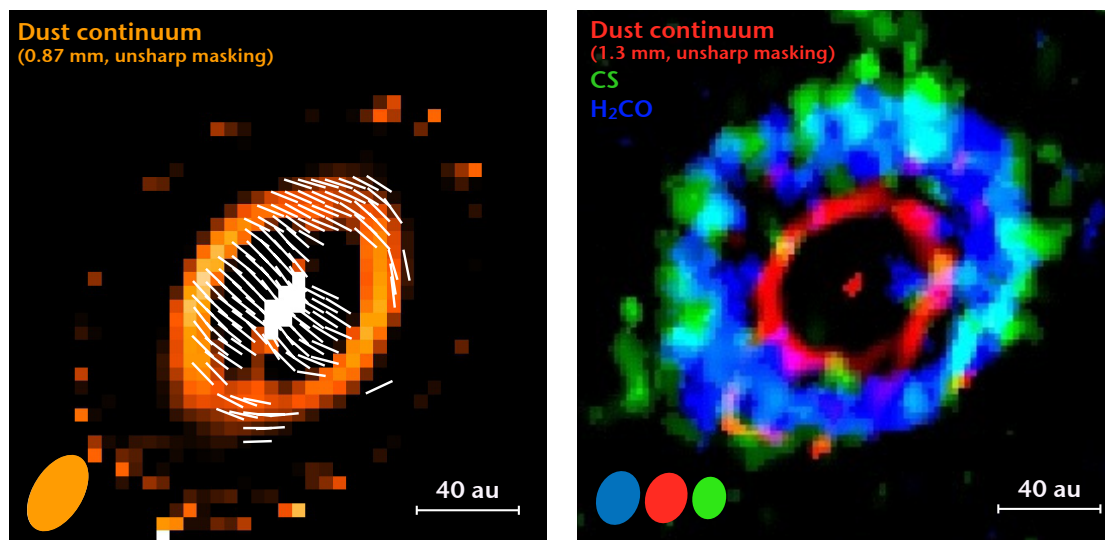


**Fig. 4.** *Left panel:* continuum map at 0.87 mm after unsharp masking is compared with the orientation of the linear polarization vectors at 0.87 mm (Bacciotti et al. 2018). The orange ellipse on the bottom left corner indicates the synthesized beam of the 0.87 mm continuum. *Right panel:* the RGB image shows the continuum at 1.3 mm after unsharp masking (in red),  $\text{H}_2\text{CO}$   $3_{1,2} - 2_{1,1}$  (in blue), and CS  $5 - 4$  (in green). The blue, red, and green ellipses on the bottom left corner indicate the synthesized beam for  $\text{H}_2\text{CO}$ , continuum, and CS, respectively.

the Sz 71 and Sz 68 disks in Lupus (van Terwisga et al. 2019). As discussed by Cazzoletti et al. (2018) the main reactions that form CN start from  $\text{H}_2^*$ , i.e.  $\text{H}_2$  molecules that are pumped into excited vibrational states by far-ultraviolet (FUV) radiation. The reaction  $\text{N} + \text{H}_2^* \rightarrow \text{NH} + \text{H}$  is followed by  $\text{C}^+ + \text{NH} \rightarrow \text{CN}^+ + \text{H}$ , and  $\text{CN}^+$  finally goes to CN through a charge transfer with H, or following dissociative recombination of the intermediates  $\text{HCN}^+$  and  $\text{HCNH}^+$ . As the abundance of  $\text{H}_2^*$  strongly depends on the FUV radiation, CN could be a good tracer of the outer disk surface layers which are more strongly exposed to intense FUV irradiation, as predicted by disk thermo-chemical models (Cazzoletti et al. 2018; Fedele & Favre 2020), and in agreement with the CN ring-like morphology detected in the disks of TW Hya, Sz 71, and Sz 68 (Hily-Blant et al. 2017; van Terwisga et al. 2019). A recent study by Arulanantham et al. (2020), however, shows that the intensity of the CN lines detected at mm wavelengths are anticorrelated with the FUV continuum measured from the HST spectra. This may be due to the fact that if on the one hand FUV irradiation promotes CN formation due to increased production of  $\text{H}_2^*$  and atomic N, on the other hand it also increases CN destruction. In this light, in the case of DG Tau the detected CN emission could originate mostly from the circumstellar envelope, and only in little part from the UV irradiated outer disk layers.

## 5. Conclusions

ALMA observations at  $0''.15$  resolution of the disk of DG Tau show that  $\text{H}_2\text{CO}$  and CS emission originates from a disk ring located at the edge of the 1.3 mm dust continuum ( $R_{\text{dust}} \sim 66$  au), with the peak of CS emission at  $\sim 70$  au, i.e. slightly outside the  $\text{H}_2\text{CO}$  peak at  $\sim 60$  au. The fact that  $\text{H}_2\text{CO}$  and CS emission are roughly co-spatial suggests that CS and  $\text{H}_2\text{CO}$  molecules are chemically linked, as both of them may be formed in gas-phase from simple radicals, and/or desorbed from dust grain mantles. Moreover, as the considered CS and  $\text{H}_2\text{CO}$  lines have similar excitation conditions it is likely that they originate from the same disk region both radially and vertically. The CN emission emerges outside the 1.3 mm dust emission ( $\sim 80$  au) and

extends out to  $\sim 500$  au. The anti-correlation between  $\text{H}_2\text{CO}$ , CS, and CN line emission and the dust continuum could be due to (i) dust opacity and/or over-subtraction of the continuum (due to optically thick circumstellar gas) which screen line emission from the inner disk; and/or (ii) the fact that the outer disk at the edge of/outside the mm dust is more exposed to UV radiation which may enhance the abundance of simple radicals, atomic O, and  $\text{H}_2^*$ , hence gas-phase formation of CS,  $\text{H}_2\text{CO}$ , and CN, as well as photodesorption of molecules from grains. Some features of the observed molecular emission, i.e. the co-spatiality of  $\text{H}_2\text{CO}$  and CS emission, CN emission extending out to larger radii, is in agreement with the predictions of thermo-chemical models (Cazzoletti et al. 2018; Fedele & Favre 2020). After unsharp masking the continuum at 0.87 mm and 1.3 mm shows a ring of enhanced dust emission located at  $\sim 40$  au, i.e. outside the CO snowline ( $\sim 30$  au). Interestingly, the peak of molecular emission is just outside this ring of enhanced dust emission where we also observe a change of the orientation of the linear polarization at 0.87 mm. This suggests a change of the dust properties outside the CO snowline and a link between the observed molecular emission and the dust properties.

**Acknowledgements.** This paper uses ALMA data from project 2016.1.00846.S (PI: L. Podio). ALMA is a partnership of ESO (representing its member states), NSF (USA) and NINS (Japan), together with NRC (Canada), MOST and ASIAA (Taiwan), and KASI (Republic of Korea), in cooperation with the Republic of Chile. The Joint ALMA Observatory is operated by ESO, AUI/NRAO and NAOJ. This work was partly supported by PRIN-INAF/2016 GENESIS-SKA and by the Italian Ministero dell'Istruzione, Università e Ricerca, through the grants Progetti Premiali 2012/iALMA (CUP-C52I13000140001), 2017/FRONTIERA (CUP-C61I15000000001), SIR-(RBSI14ZRRH), and by the European MARIE SKŁODOWSKA-CURIE ACTIONS under the European Union's Horizon 2020 research and innovation programme, for the Project "Astro-Chemistry Origins" (ACO), Grant No 811312. CC, CF, and EB acknowledge funding from the European Research Council (ERC) under the European Unions Horizon 2020 research and innovation programme, for the Project The Dawn of Organic Chemistry (DOC), grant agreement No 741002. CF also acknowledges financial support from the French National Research Agency in the framework of the Investissements d'Avenir program (ANR-15-IDEX-02), through the funding of the "Origin of Life" project of the Univ. Grenoble-Alpes.



## References

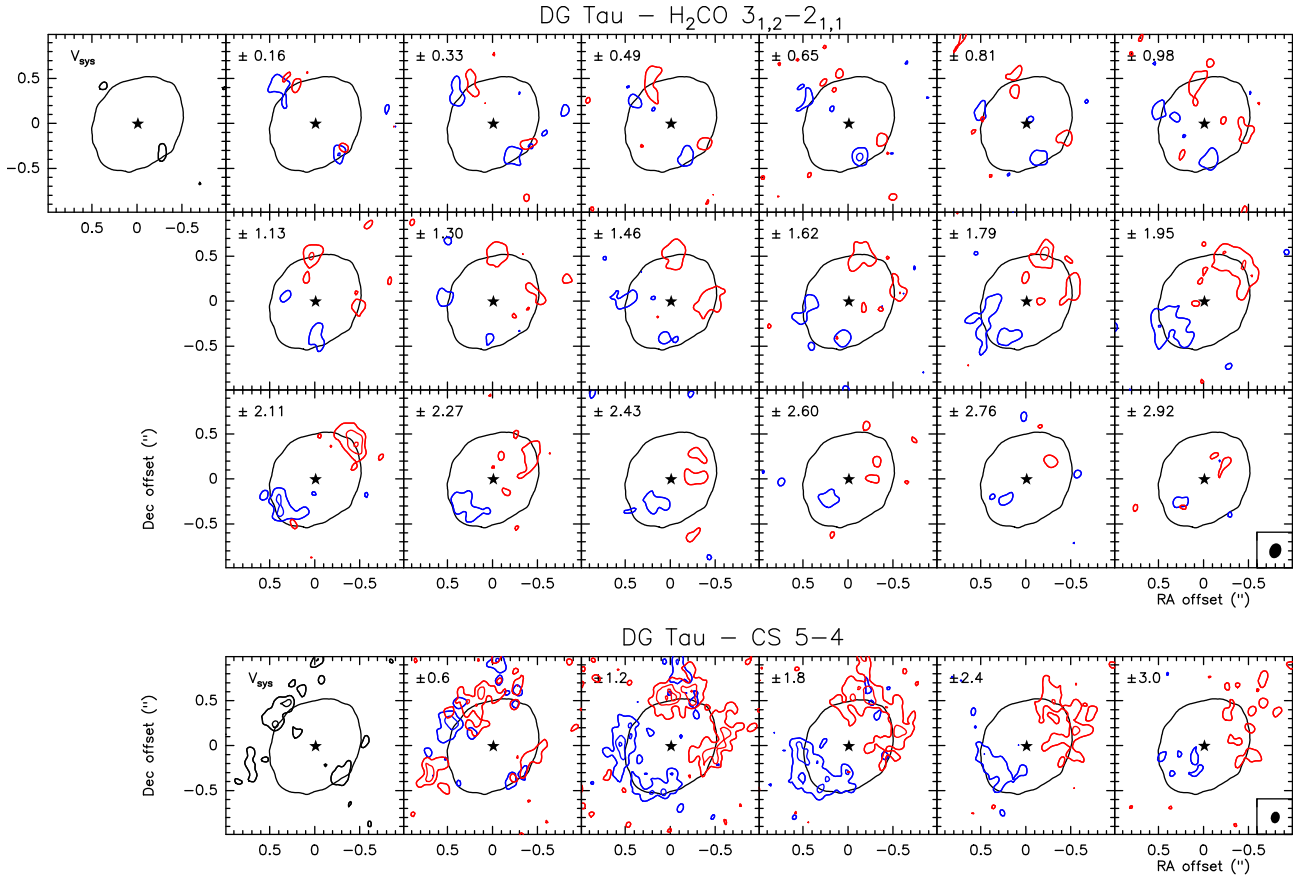
- ALMA Partnership, Brogan, C. L., Pérez, L. M., et al. 2015, *ApJ*, 808, L3
- Andrews, S. M., Huang, J., Pérez, L. M., et al. 2018, *ApJ*, 869, L41
- Arulanantham, N., France, K., Cazzoletti, P., et al. 2020, *AJ*, 159, 168
- Bacciotti, F., Girart, J. M., Padovani, M., et al. 2018, *ApJ*, 865, L12
- Bacciotti, F., Mundt, R., Ray, T. P., et al. 2000, *ApJ*, 537, L49
- Beckwith, S. V. W., Sargent, A. I., Chini, R. S., & Guesten, R. 1990, *AJ*, 99, 924
- Bergin, E. A., Du, F., Cleaves, L. I., et al. 2016, *ApJ*, 831, 101
- Bergner, J. B., Guzmán, V. G., Öberg, K. I., Loomis, R. A., & Pegues, J. 2018, *ApJ*, 857, 69
- Bergner, J. B., Öberg, K. I., Bergin, E. A., et al. 2019, *ApJ*, 876, 25
- Booth, A. S., Walsh, C., & Ilee, J. D. 2019a, *A&A*, 629, A75
- Booth, A. S., Walsh, C., Ilee, J. D., et al. 2019b, *ApJ*, 882, L31
- Carney, M. T., Fedele, D., Hogerheijde, M. R., et al. 2018, *A&A*, 614, A106
- Carney, M. T., Hogerheijde, M. R., Guzmán, V. V., et al. 2019, *A&A*, 623, A124
- Carney, M. T., Hogerheijde, M. R., Loomis, R. A., et al. 2017, *A&A*, 605, A21
- Cazzoletti, P., van Dishoeck, E. F., Visser, R., Facchini, S., & Bruderer, S. 2018, *A&A*, 609, A93
- de Valon, A., Dougados, C., Cabrit, S., et al. 2020, *A&A*, 634, L12
- Eisloffel, J. & Mundt, R. 1998, *AJ*, 115, 1554
- Favre, C., Fedele, D., Maud, L., et al. 2019, *ApJ*, 871, 107
- Favre, C., Fedele, D., Semenov, D., et al. 2018, *ApJ*, 862, L2
- Fedele, D., Bruderer, S., van Dishoeck, E. F., et al. 2013, *A&A*, 559, A77
- Fedele, D., Carney, M., Hogerheijde, M. R., et al. 2017, *A&A*, 600, A72
- Fedele, D. & Favre, C. 2020, *A&A*, 638, A110
- Fedele, D., Tazzari, M., Booth, R., et al. 2018, *A&A*, 610, A24
- Gaia Collaboration, Brown, A. G. A., Vallenari, A., et al. 2018, *A&A*, 616, A1
- Gaia Collaboration, Prusti, T., de Bruijne, J. H. J., et al. 2016, *A&A*, 595, A1
- Garufi, A., Podio, L., Codella, C., et al. 2020, *A&A*, 636, A65
- Garufi, A., Quanz, S. P., Schmid, H. M., et al. 2016, *A&A*, 588, A8
- Güdel, M., Eibensteiner, C., Dionatos, O., et al. 2018, *A&A*, 620, L1
- Guilloteau, S., Di Folco, E., Dutrey, A., et al. 2013, *A&A*, 549, A92
- Guzmán, V. V., Öberg, K. I., Carpenter, J., et al. 2018, *ApJ*, 864, 170
- Hily-Blant, P., Magalhaes, V., Kastner, J., et al. 2017, *A&A*, 603, L6
- Huang, J., Öberg, K. I., & Andrews, S. M. 2016, *ApJ*, 823, L18
- Huang, J., Öberg, K. I., Qi, C., et al. 2017, *ApJ*, 835, 231
- Isella, A., Guidi, G., Testi, L., et al. 2016, *Phys. Rev. Lett.*, 117, 251101
- Isella, A., Natta, A., Wilner, D., Carpenter, J. M., & Testi, L. 2010, *ApJ*, 725, 1735
- Kastner, J. H., Qi, C., Dickson-Vandervelde, D. A., et al. 2018, *ApJ*, 863, 106
- Kastner, J. H., Qi, C., Gorti, U., et al. 2015, *ApJ*, 806, 75
- Kitamura, Y., Kawabe, R., & Saito, M. 1996, *ApJ*, 457, 277
- Le Gal, R., Öberg, K. I., Loomis, R. A., Pegues, J., & Bergner, J. B. 2019, *ApJ*, 876, 72
- Lee, J.-E., Lee, S., Baek, G., et al. 2019, *Nature Astronomy*, 3, 314
- Loomis, R. A., Cleaves, L. I., Öberg, K. I., Guzman, V. V., & Andrews, S. M. 2015, *ApJ*, 809, L25
- Loomis, R. A., Öberg, K. I., Andrews, S. M., et al. 2020, *ApJ*, 893, 101
- Mathews, G. S., Klaassen, P. D., Juhász, A., et al. 2013, *A&A*, 557, A132
- Müller, H. S. P., Thorwirth, S., Roth, D. A., & Winnewisser, G. 2001, *A&A*, 370, L49
- Öberg, K. I., Furuya, K., Loomis, R., et al. 2015a, *ApJ*, 810, 112
- Öberg, K. I., Guzmán, V. V., Furuya, K., et al. 2015b, *Nature*, 520, 198
- Öberg, K. I., Guzmán, V. V., Merchantz, C. J., et al. 2017, *ApJ*, 839, 43
- Pegues, J., Öberg, K. I., Bergner, J. B., et al. 2020, *ApJ*, 890, 142
- Penteado, E. M., Walsh, C., & Cuppen, H. M. 2017, *ApJ*, 844, 71
- Pérez, L. M., Carpenter, J. M., Andrews, S. M., et al. 2016, *Science*, 353, 1519
- Phuong, N. T., Chapillon, E., Majumdar, L., et al. 2018, *A&A*, 616, L5
- Podio, L., Bacciotti, F., Fedele, D., et al. 2019, *A&A*, 623, L6
- Podio, L., Garufi, A., Codella, C., et al. 2020, *arXiv e-prints*, arXiv:2008.12648
- Podio, L., Kamp, I., Codella, C., et al. 2013, *ApJ*, 766, L5
- Podio, L., Kamp, I., Flower, D., et al. 2012, *A&A*, 545, A44
- Qi, C., Öberg, K. I., & Wilner, D. J. 2013a, *ApJ*, 765, 34
- Qi, C., Öberg, K. I., Wilner, D. J., et al. 2013b, *Science*, 341, 630
- Quanz, S. P., Schmid, H. M., Geissler, K., et al. 2011, *ApJ*, 738, 23
- Schuster, K. F., Harris, A. I., Anderson, N., & Russell, A. P. G. 1993, *ApJ*, 412, L67
- Sheehan, P. D. & Eisner, J. A. 2017, *ApJ*, 840, L12
- Sheehan, P. D. & Eisner, J. A. 2018, *ApJ*, 857, 18
- Shirley, Y. L. 2015, *PASP*, 127, 299
- Teague, R., Henning, T., Guilloteau, S., et al. 2018, *ApJ*, 864, 133
- Testi, L., Bacciotti, F., Sargent, A. I., Ray, T. P., & Eisloffel, J. 2002, *A&A*, 394, L31
- van 't Hoff, M. L. R., Tobin, J. J., Trapman, L., et al. 2018, *ApJ*, 864, L23
- van Terwisga, S. E., van Dishoeck, E. F., Cazzoletti, P., et al. 2019, *A&A*, 623, A150
- Wakelam, V., Loison, J. C., Mereau, R., & Ruaud, M. 2017, *Molecular Astrophysics*, 6, 22
- Walsh, C., Loomis, R. A., Öberg, K. I., et al. 2016, *ApJ*, 823, L10
- Walsh, C., Millar, T. J., Nomura, H., et al. 2014, *A&A*, 563, A33
- Willacy, K. & Woods, P. M. 2009, *ApJ*, 703, 479
- Zhang, K., Schwarz, K. R., & Bergin, E. A. 2020, *ApJ*, 891, L17

## Appendix A: Channel maps

The channel maps of the  $\text{H}_2\text{CO } 3_{1,2} - 2_{1,1}$ ,  $\text{CS } 5 - 4$ , and  $\text{CN } 2 - 1$  emission towards DG Tau are presented in Fig. [A.1](#) and [A.2](#).

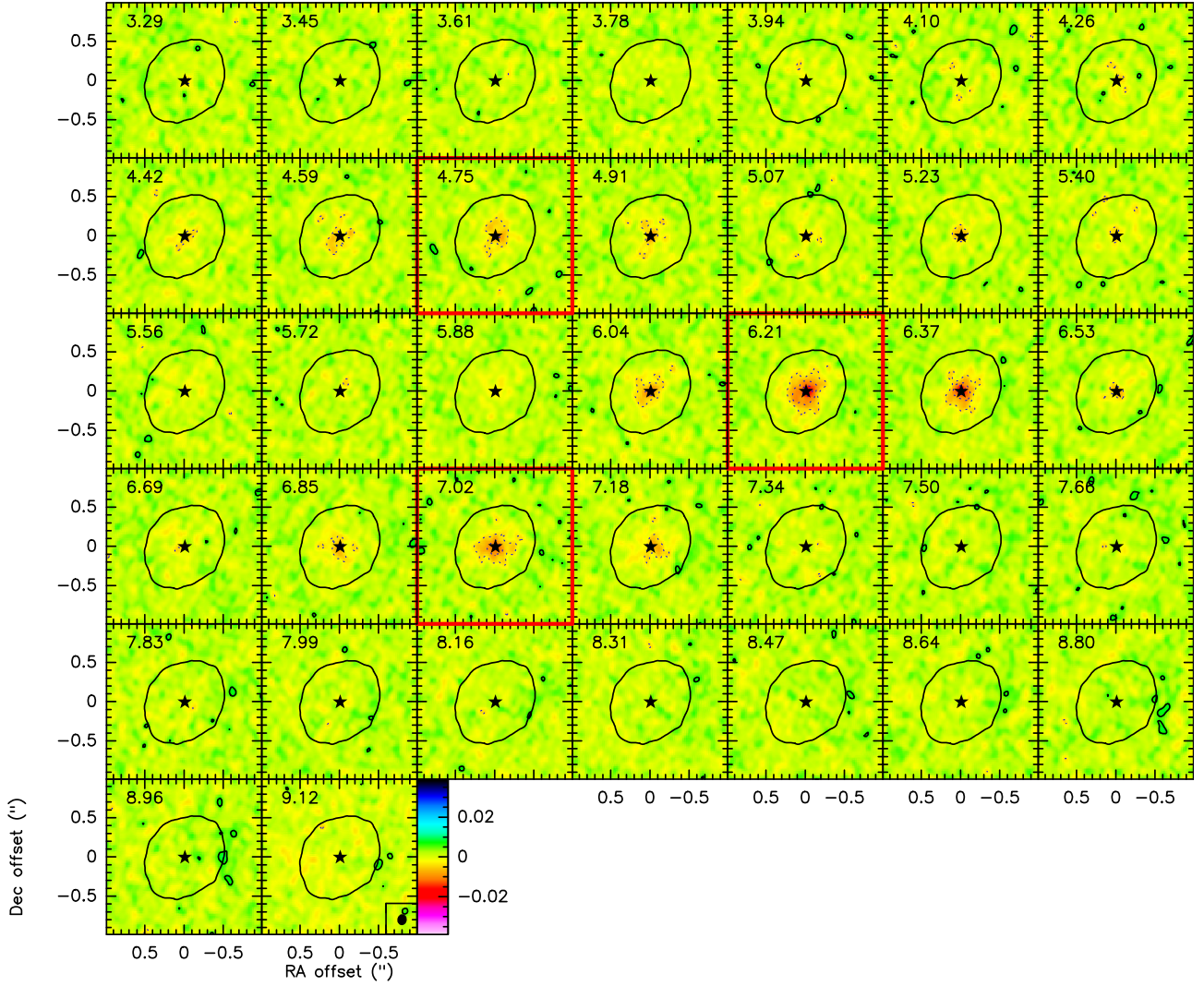
## Appendix B: Integrated spectra in brightness temperature

The line spectra shown in Fig. [3](#) obtained by integrating the line cube over a disk ring extending from  $0''.33$  to  $0''.75$  and over a circular area of  $3''$  are converted in brightness temperature  $T_{\text{B}}$  as shown in Fig. [B.1](#).



**Fig. A.1.** Channel maps of  $\text{H}_2\text{CO}$   $3_{1,2} - 2_{1,1}$  and CS  $5 - 4$  emission towards DG Tau. The blue and red contours show the emission at symmetric blue- and red-shifted velocities with respect to systemic ( $V_{\text{sys}} = +6.24$  km s $^{-1}$ ) up to  $V - V_{\text{sys}} = \pm 3$  km s $^{-1}$ , as labeled in the upper left corner of each channel box. The  $\text{H}_2\text{CO}$   $3_{1,2} - 2_{1,1}$  and CS  $5 - 4$  lines are observed in the narrow (0.162 km s $^{-1}$  per channel) and broad (0.6 km s $^{-1}$  per channel) spectral window, respectively. First contour and step are  $3\sigma$ . The black star and contour indicates the peak and the  $5\sigma$  level of the 1.3 mm continuum. The ellipse in the bottom right corner of the last channel shows the ALMA synthesized beam.



DG Tau – CN 2–1,  $J=5/2-3/2$ ,  $F=7/2-3/2$ 

**Fig. A.2.** Channel maps of CN 2 – 1 emission towards DG Tau. The channel velocity,  $V_{\text{LSR}}$ , is relative to the brightest CN 2 – 1,  $J=5/2-3/2$ ,  $F=7/2-3/2$  hyperfine component and is labeled in the upper left corner of each channel box. The other two hyperfine components are offset by  $-1.47 \text{ km s}^{-1}$  and  $+0.78 \text{ km s}^{-1}$  with respect to the brightest one (see Table 1). The channels corresponding to the systemic velocity for the three hyperfine components (i.e.  $6.21 \text{ km s}^{-1}$ ,  $4.75 \text{ km s}^{-1}$ , and  $7.02 \text{ km s}^{-1}$ ) are highlighted by a thick red box. First contour and step are  $3\sigma$ , negative intensities are shown by dashed contours. The black star and contour indicates the peak and the  $5\sigma$  level of the 1.3 mm continuum. The ellipse in the bottom right corner of the last channel shows the ALMA synthesized beam.

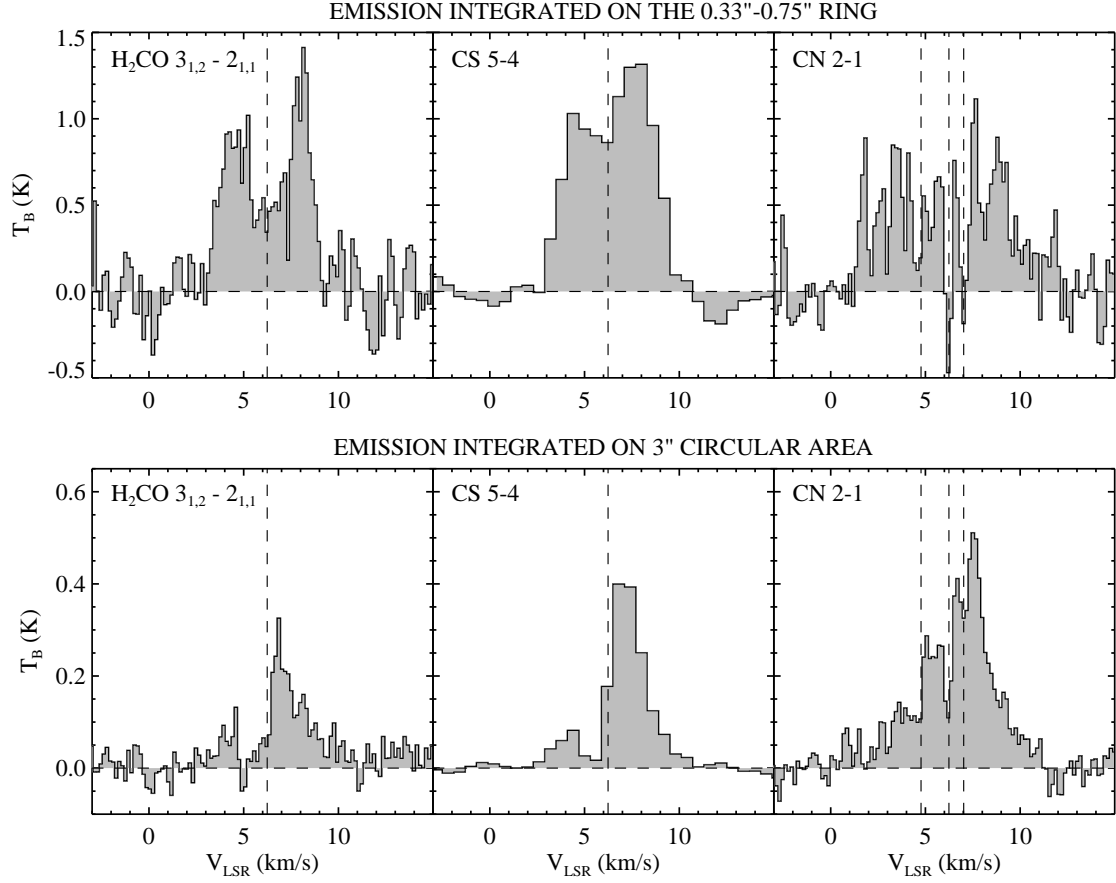


**Fig. B.1.**  $\text{H}_2\text{CO } 3_{1,2} - 2_{1,1}$ , CS 5 – 4, and CN 2 – 1 spectra integrated over a  $0.33'' - 0.75''$  ring area (top panels) and over a  $3''$  circular area (bottom panels), in brightness temperature  $T_B$ . The vertical dashed lines indicate the systemic velocity,  $V_{\text{sys}} = +6.24 \text{ km s}^{-1}$ . For CN 2 – 1 the velocity scale corresponds to the brightest of the three hyperfine components at 226.87 GHz reported in Table 1 ( $N = 2 - 1$ ,  $J = 5/2 - 3/2$ ,  $F = 7/2 - 3/2$ ), and the position of the two fainter components is indicated by the vertical dashed lines.